Journal of Materials Chemistry B

ROYAL SOCIETY OF CHEMISTRY

PAPER

View Article Online
View Journal | View Issue

Cite this: J. Mater. Chem. B, 2022, 10, 8450

A green flexible and wearable biosensor based on carbon nanofibers for sensitive detection of uric acid in artificial urine†

Hao Zheng,[abc] Xiao Han,[bc] Qiulin Wei,[bc] Xinliang Liu,[a] Yao Li *[abc] and Jinghui Zhou *[bc]

Wearable biosensors have great advantages and application potential in the field of real-time detection. However, it is still a challenge to construct an electrically conductive and mechanically flexible sensing interface as the working electrode in an electrochemical sensor. In this work, a green and efficient strategy is proposed to optimize the chemical structure of precursor materials for the preparation of a flexible biosensor. The introduction of phosphated lignin effectively increases the molecular interaction in the electrospinning system, improving the micro-morphology, flexibility, and thermal stability of biomass-based carbon nanofibers (CNFs). The rich active sites and high graphitization degree provide abundant access to uric acid molecules and accelerate electron transmission. Benefiting from these compelling features, the fabricated wearable biosensor can accurately and selectively detect uric acid in artificial urine. This work offers a promising approach for the fabrication of wearable biosensors and has a broad application prospect in personalized diagnostic and miniaturized power device fields.

Received 21st July 2022,
Accepted 14th September 2022

DOI: 10.1039/d2tb01547a

rsc.li/materials-b

1. Introduction

The traditional healthcare security system is mainly passive, expensive and disease-centered treatment oriented. Most patients visit a doctor only when they feel physical discomfort or when obvious symptoms appear.[1,2] Diagnosis in hospitals usually requires complex instrumentation, which is expensive and time-consuming.[3,4] People with underlying diseases and unsubstantial medical awareness often choose to self-medicate and fail to receive timely diagnosis and treatment, increasing the risk of disease progression.[5–7] This traditional medical model does not allow individuals to participate in the monitoring of their own health, which is not conducive to the early diagnosis and predictive analysis of diseases.[8–11] In addition, with the outbreak of the coronavirus disease in 2019 (COVID-19), the diagnostic steps are more complicated.[9] It is particularly important to realize personal health monitoring at home to meet the needs of users to acquire dynamic physiological state actively in time and achieve personalized medicine.

Flexible and wearable biosensors have attracted much attention due to their high ductility, good biocompatibility, low cost and light weight.[12–14] The sensors can be conformally concatenated on irregular surfaces to convert surface deformations into electrical signals, showing great potential in the field of electronic skin, human–computer interaction and personal health monitoring.[3,9,15] Urine is a liquid excreted from the body during metabolism, which is closely related to our nervous, digestive and urinary systems.[5] Urine can be easily collected and stored usually as an ideal analytical solution for non-invasive wearable monitoring devices, which can accurately and continuously reflect different kinds of physiological signals.[8,9] This wearable detection method allows us to monitor the dynamic changes of physical activities and vital signs at any time, thus solving the limitations of passive medical treatment.[3,16,17] The preparation of working electrode materials is a key factor for determining the sensing performance of wearable biosensors. Typically, the electrodes are composed of noble metals (platinum or gold) attached to flexible substrates, such as polyethylene terephthalate (PET), polyvinylidene fluoride (PVDF) or polydimethylsiloxane (PDMS).[11,18–20] Although these biosensor materials have high conductivity, due to the poor permeability it is difficult for them to meet the requirements of body heat and humidity comfort.[4,6,21] Considering that the intimate contact between the closed working electrode and human skin will destroy the dynamic balance of heat dissipation,

[a] Guangxi Key Laboratory of Clean Pulp & Papermaking and Pollution Control, College of Light Industry and Food Engineering, Guangxi University, Nanning 530004, P. R. China. E-mail: liyaodlpu@163.com, zhoujh@dlpu.edu.cn
[b] Collaborative Innovation Center for Lignocellulosic Biorefinery, Dalian, Liaoning Province, 116034, P. R. China
[c] College of Light Industry and Chemical Engineering, Dalian, Liaoning Province, 116034, P. R. China

† Electronic supplementary information (ESI) available. See DOI: https://doi.org/10.1039/d2tb01547a

wearing biosensors for a long time will lead to allergic reactions such as skin pruritus.[7,22,23] Therefore, exploring more comfortable and breathable conductive materials for preparing working electrodes is an important task for the manufacture of breathable flexible urine biosensors.

Carbon nanofibers (CNFs) have attracted extensive attention in the field of breathable biosensors due to their excellent flexibility, high porosity and inherent conductivity.[24–27] However, most CNFs use petroleum-based raw materials as spinning auxiliary, which limits their large-scale application. In this work, a green and efficient strategy is proposed to optimize the chemical structure of precursor materials to prepare flexible biomass-based CNFs by electrospinning. The introduction of phosphated lignin effectively increases the molecular interaction in the electrospinning system, which is of great significance for the successful preparation and characteristic formation of biomass-based CNFs. This simple and green method effectively avoids the microstructure collapse for the biomass-based CNFs in the carbonization process. The obtained biomass-based CNFs exhibit good flexibility, large specific surface area and a regular graphite structure providing rich active sites for biomarkers, which accelerates the transfer of electrons in urine. The prepared CNFs can be used as the working electrode material for wearable biosensors, which provide a research basis for long-term disease diagnosis, physiological evaluation and family health monitoring.

2. Experimental section

2.1 Materials

Poplar lignin powder was generously provided by Dongsheng New Material Co., Ltd (Shanghai, China). Cellulose acetate (CA, M_w = 30 000) was purchased from Sigma-Aldrich (Shanghai, China). Acetone and *N*,*N*-dimethylacetamide were purchased from Ruizheng Chemical Technology Co., Ltd (Shanghai, China). Phosphoric acid (H_3PO_4) was purchased from Kemiou Chemical Reagent Factory (Tianjin, China). Artificial urine (including creatinine) was purchased from Shanghai Xinfan Biotechnology Co., Ltd. Ascorbic acid, glucose and tyrosine were added according to the analyte content of human urine. All chemicals were used as received.

2.2 Preparation of biomass-based carbon nanofibers

2 g of poplar lignin powder was first added to the mixture of acetone and *N*,*N*-dimethylacetamide (12 mL, AC/DMAC = 1 : 1) and stirred at room temperature for 40 min. 0.8 g of phosphoric acid was mixed dropwise and stirred at 60 °C for 2 h to obtain phosphorylated lignin. Subsequently, 2 g of CA was mixed and stirred at 60 °C for 24 h. This mixture was used as the spinning solution to prepare precursor nanofibers (PFs) by electrospinning. The working voltage of electrospinning is 20 kV (+15 kV and −5 kV), and the feed roller distance and speed are 18 cm and 0.8 ml h^{-1}, respectively. The PFs were treated in a tube furnace (GSL-1700X, Hefei Kejing Materials Technology Co., Ltd, China) at 200 °C with a heating rate of 0.4 °C min^{-1} for 12 h, aiming to acquire the stabilized nanofibers (SFs). Finally, the carbon nanofibers (CNFs) were acquired by heating to 800 °C at a rate of 2.0 °C min^{-1} and carbonizing at 800 °C for 180 min under a NH_3 atmosphere.

Three kinds of PF samples were prepared: PFs-1 (phosphorylated lignin : CA = 3 : 7), PFs-2 (phosphorylated lignin : CA = 5 : 5) and PFs-3 (phosphorylated lignin : CA = 7 : 3). The CNFs were obtained by heating at 800 °C for 3 h and named CNFs-1, CNFs-2 and CNFs-3, respectively.

2.3 Characterization

The chemical bond composition of samples was measured with an FT-IR spectrophotometer (PEINC., the United States) and the spectrum range was from 4000 to 400 cm^{-1}. The micromorphology characterization of the PFs and CNFs was performed by scanning electron microscopy (SEM, JEOL JSM 7800F). The thermal stability of the precursor fibers was tested by thermogravimetric analysis (TGA) (TGA 5500IR, TA Instruments). 5 mg of samples were loaded in alumina pans and heated from 10 to 700 °C with a heating rate of 10 °C min^{-1} under a nitrogen atmosphere. Differential scanning calorimetry (DSC) analysis was performed using a Discovery DSC 250. The phase structure of the sample was examined by X-ray diffraction (XRD-7000S). The graphitization structures of CNFs were measured using a Raman spectrometer (Renishaw Co., UK). The N_2 adsorption–desorption isotherms and Brunauer–Emmett–Teller (BET) analysis of CNFs were examined using an ASAP 2020 PLUS HD88. The surface wettability of the carbon nanofibers was examined using a contact angle goniometer (SL200B). X-ray photoelectron spectrometry (XPS) was performed using a Thermo ESCALAB 250 spectrometer (USA). The electrodes prepared using free-standing carbon materials avoid the requirement of loading binders or conductive additives. The mass of CNFs is determined with an electronic balance (analytical grade). All the electrochemical analysis was performed using three electrode systems (CHI 660, CH Instruments Inc, USA). The electrical conductivity of the CNFs was tested using a two-point probe (Keithley 2000 multimeter). The mechanical properties were determined using a Zwick Z_2 tensile instrument on CNFs 4 cm in length.

3. Results and discussion

The reaction equation of phosphoric acid for lignin and CA and the formation mechanism of the biomass-based CNFs are shown in Scheme 1. Phosphoric acid molecules react with hydroxyl groups of lignin and CA to form phospholipid bonds. These phospholipid bonds effectively connect lignin and CA, leading to the combination of lignin's good thermal stability and CA's good processing ability. Furthermore, these phospholipid bonds can effectively reduce the existence of free CA, thus reducing the phase separation in the spinning solution due to the difference in the chemical structure of lignin and CA. With the decrease of phase separation, the spinnability of precursor materials becomes more uniform, and the fine fibers and bead like structural defects in the morphology of the obtained CNFs are effectively reduced. The complete and uniform fiber

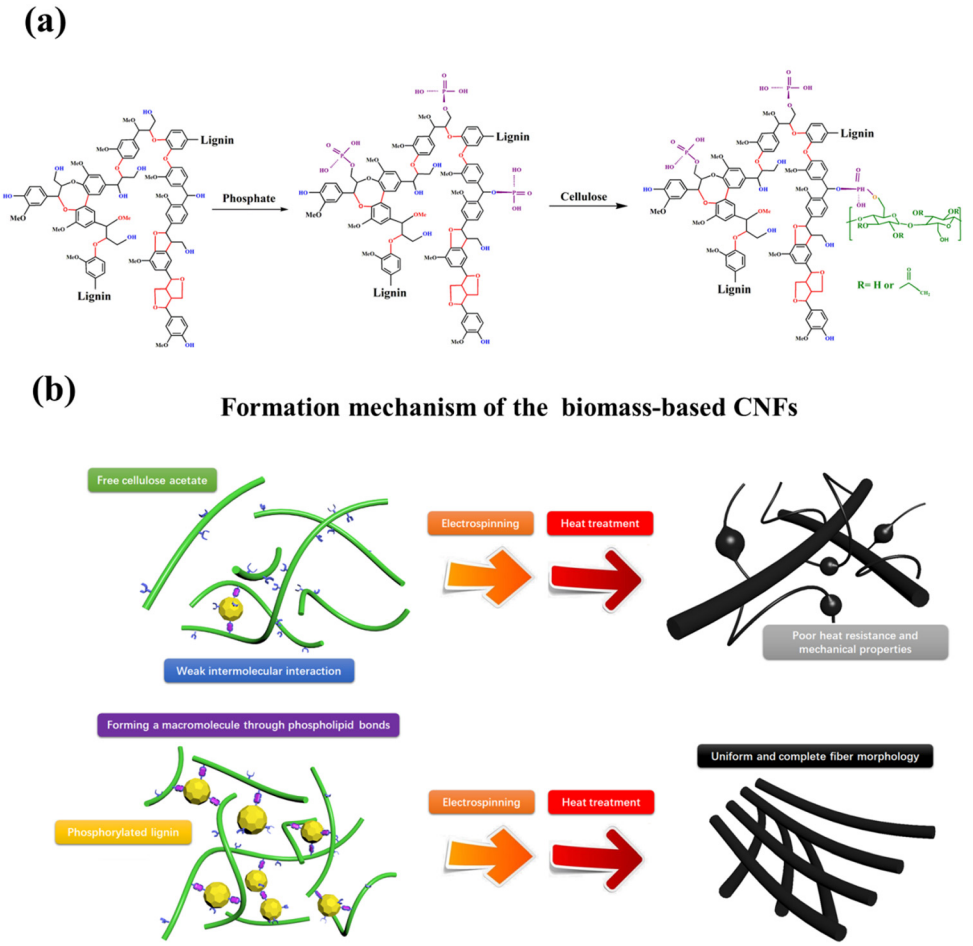

Scheme 1 (a) The reaction equation of phosphoric acid for lignin and CA, and (b) the formation mechanism of the biomass-based CNFs.

morphologies are of great value for improving the overall performances of biomass-based CNFs.

The precursor materials of PFs-1, PFs-2 and PFs-3 are determined by FTIR and the IR spectra are shown in Fig. 1(a). The stretching vibration peaks of the hydroxyl group appear at 3435 cm^{-1}. The peaks at around 2939 and 2837 cm^{-1} are caused by the C–H stretching vibration of $–CH_3$ and $–CH_2$ groups. The peak at 1752 cm^{-1} is attributed to the carbonyl stretching vibration of CA. The typical peaks of the aromatic ring vibration for lignin are at 1614, 1513 and 1460 cm^{-1}. And the characteristic peaks of phospholipid groups are observed at 1100 cm^{-1}. These gradually increasing signal peaks are closely related to the increase of the phosphorylated lignin ratio proportion. For comparison, the FTIR of raw lignin and phosphorylated lignin are measured as shown in Fig. S1 (ESI†). The range of deformation vibration at the lignin aromatic skeleton is enlarged, which is attributed to the formation of the P–O bond.

Thermodynamic behavior of precursor materials plays an important role in the hot working process of carbon materials. High glass transition temperatures can effectively maintain the microstructure of carbon materials, resulting in a larger specific surface.[28,29] Thermodynamic behaviors of PFs-1, PFs-2 and PFs-3 are determined by DSC, and they show only one obvious glass transition platform (Fig. 1(b)). This phenomenon implies that lignin and CA have been linked through the phospholipid bond. The glass transition temperatures of PFs-1, PFs-2 and PFs-3 are 152, 161, and 171 °C, respectively. With the increased content of phosphorylated lignin, the glass transition temperature of the precursor materials increases gradually. A sufficiently high glass transition temperature can protect nanofibers from fusing and softening in the thermo-stabilization process. The high carbon content and low oxygen elemental content of lignin are the basic requirements for the preparation of excellent precursors of various carbon materials. To further quantify the degree of phosphorylation by elemental analysis, as shown in Table S1 (ESI†). The carbon elemental content of all samples reaches a high value (more than 45%). Compared with other samples, PFs-3 exhibits the highest carbon content (50.7%) and the lowest oxygen content (42.11%). The high phosphorylated lignin content is conducive to reducing the autoxidation weightlessness of the precursor fibers, thereby effectively maintaining the morphology of biomass-based CNFs.

The TGA and DTG curves of the precursor materials are depicted in Fig. 1(c). These precursor materials begin to decompose at 190 °C and exhibit the maximum weight loss rate at 240 °C. The initial weightlessness stage is mainly due to the

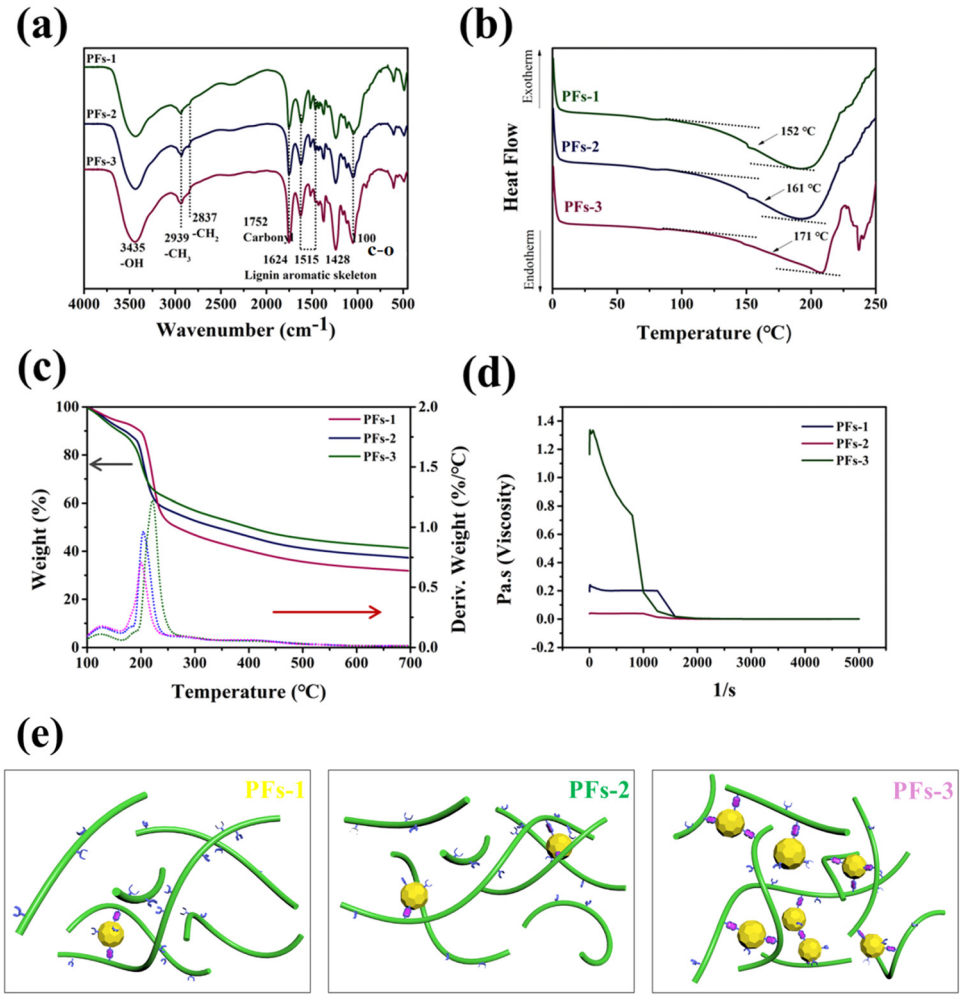

Fig. 1 Basic properties of precursor nanofiber samples (a) FTIR spectra, (b) DSC spectra, (c) TGA, (d) viscosity curve of the free-standing carbon nanofibers, and (e) the mechanism of the phosphorylation process.

escape stage of small molecules or the induction stage of the thermal decomposition reaction. The main reactions are intramolecular disturbance and chemical bond breaking induced by active functional groups. The second weightlessness stage occurs in the temperature range of 190–260 °C, which is ascribed to the depolymerization reactions of CA and the cleavage of the ether bond between the lignin structural units. Subsequently, the main reaction types of the third weightlessness stage (400–700 °C) are attributed to methoxide hemolysis and rearrangement of the aromatic ring. With the increase of phosphorylated lignin content, the weight-loss-rate ® of the precursor materials obviously decreases, and the amount of char residue slowly reduces. For a thermal treatment directly up to 700 °C, the carbon yields of PFs-1, PFs-2 and PFs-3 are 32%, 38% and 41%, respectively. Interestingly, although PFs-3 achieves the highest carbon yield, its maximum degradation rate occurs at a lower temperature (197 °C) compared with PFs-1 and PFs-2 (230 °C and 201 °C). This phenomenon is attributed to the dehydration reaction between bio-macromolecules induced by the introduction of phosphoric acid, resulting in the formation of a closer cross-linking structure between bio-macromolecules. This cross-linking structure is responsible for the excellent thermodynamic stability of PFs-3 at high temperatures.

In order to further prove the composition of phospholipid bonds between lignin and CA, the viscosity of the precursor materials is characterized. The viscosity of the polymer system reflects the intermolecular interaction and molecular weight of the polymer. With the increase of the phosphorylated lignin content, the viscosity of the system increases obviously (Fig. 1(d)). This result shows that the introduction of phosphoric acid effectively increases the interaction of macromolecules in the system. At the same time, with the formation of phospholipid bonds, the molecular weight of macromolecules in the system also increases significantly. The mechanism of this process is shown in Fig. 1(e). Phosphorylated lignin molecules act as a cross-linking point to link CA. With the increase of the phosphorylated lignin content, more CA molecules are linked together. This process effectively reduces the phase separation between lignin and CA.

The phospholipid bonds between lignin and CA have been proved in our previous work. The addition of phospholipid bonds can effectively increase the spinnability of bio-macromolecules.

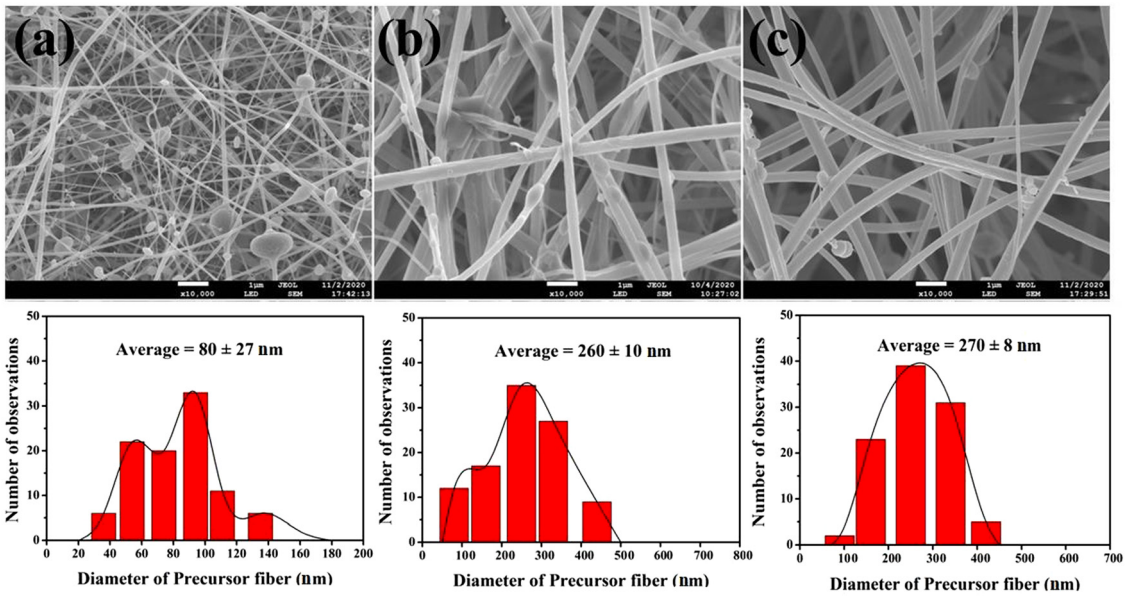

Fig. 2 SEM images and diameter distribution of precursor nanofibers prepared with different mass ratios of phosphorylated lignin to CA, (a) PFs-1, (b) PFs-2, and (c) PFs-3.

However, the role of phosphorylated lignin in the processing system is still a question. The morphologies of PFs are observed by SEM (Fig. 2(a)–(c)). PFs-1 exhibits a low fiber diameter (about 80 nm) and a large number of bead like structural defects. With the increase of the phosphorylated lignin content, these structural defects significantly reduce and the fiber diameter increases gradually. The average fiber diameters of PFs-2 and PFs-3 are 260 ± 10 and 270 ± 8 nm, respectively. Furthermore, the uniformity of the bead-free nanofibers is improved compared with that of PFs-1. This result is consistent with the mechanism diagram shown in Fig. 1(e). The unconnected CA molecules tend to form small diameter nanofibers under the action of an electric field. With the increase of the phosphorylated lignin content, CA molecules are linked together with phosphorylated lignin as the cross-linking point. This cross-linking structure effectively increases the interaction of molecules in the electrospinning system, and then the nanofibers with a large diameter are obtained. At the same time, the phase separation between lignin and CA is effectively hindered by this cross-linking structure, thus reducing the occurrence of bead like structural defects. To further prove the immiscibility between the CA and the lignin, pictures of the solution of the starting materials are analyzed (Fig. S2, ESI†). The spinning solution was tilted and allowed to stand upright, and the liquid flow and residual solution on the bottle wall were observed. It is not difficult to find that with the increase of the lignin content, the solution viscosity increases obviously, showing uniform fluidity. DSC is an accurate and simple method to explain the phase transition behavior of lignin samples (Fig. S3, ESI†). The high *Tg* of biological macromolecules means that there are fewer branched chains in their molecular structure.

High temperature heat treatment is a necessary process for the preparation of carbon materials. The good thermal stability of precursor materials not only improves the yield of carbon materials, but also effectively maintains the original morphology, thus improving the specific surface area of carbon materials.[25] The SEM spectra of CNFs are shown in Fig. 3. The phenomenon of fibers collapse and "bead" defects appear in the morphologies of CNFs-1. This is mainly attributed to the phase separation between lignin and CA. Only the phase region of lignin with excellent thermal stability effectively maintains the original morphologies, while the CA phase region could not. Therefore, morphological melt occurs in the phase region of CA. These defect morphologies are not conducive to obtaining a high specific surface area and conductivity of carbon materials, hindering the application of carbon materials in composite materials and electrochemical energy storage. With the increase of the phosphorylated lignin content, the interaction between bio-macromolecules is strengthened, reducing the appearance of phase separation. CNFs-3 exhibits a completely fibrous morphology, uniform fiber diameter and a smooth fiber surface, which are significantly positive for its application in the wearable electronic devices, supercapacitors, filtration and separation.

The microstructure of the biomass based carbon fiber is characterized by XRD (Fig. 4(a)). XRD patterns of CNFs-1, CNFs-2 and CNFs-3 show the same broad diffraction peak in the 2θ = 20–24° region. The peaks are attributed to the (002) crystallographic plane of the graphite structure, indicating a large abundance of small graphitic crystallites present in the flexible carbon nanofibers. The average interlayer spacing d_{002} is determined by the Bragg equation, the distances between interfacial microcrystalline layers of CNFs-1, CNFs-2, and CNFs-3 are calculated to be 0.380, 0.381 and 0.398 nm, respectively. The calculated interlayer spacing d_{002} of CNFs slightly increases with the increase of the phosphorylated lignin content. Another diffraction peak at 2θ = 44° appeared due to the (100) reflection. There are some impurity peaks in the XRD pattern of CNFs-1, which may be due to the

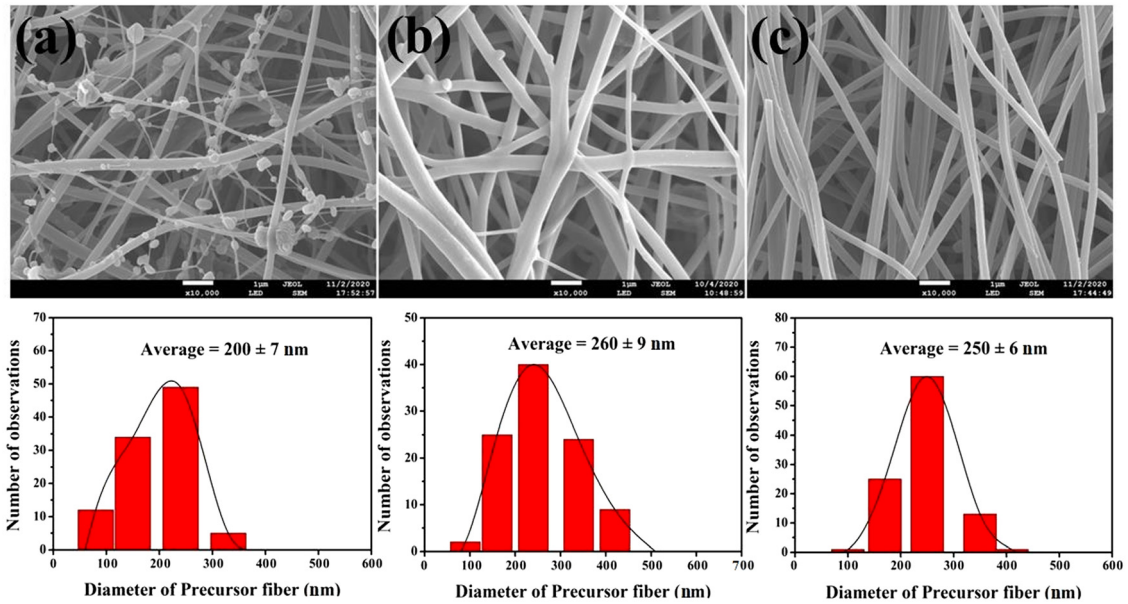

Fig. 3 SEM images and diameter distribution of carbon nanofibers prepared with different mass ratios of phosphorylated lignin to CA, (a) CNFs-1, (b) CNFs-2, and (c) CNFs-3.

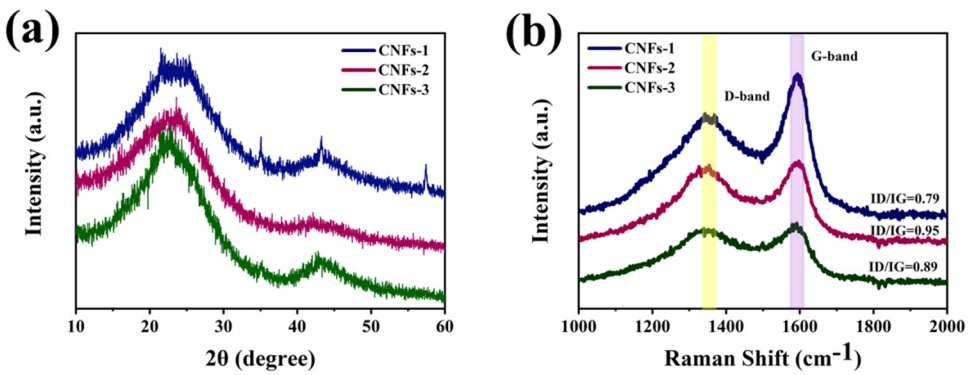

Fig. 4 (a) XRD patterns and (b) Raman spectra of the flexible CNFs prepared with different mass ratios of phosphorylated lignin to CA: CNFs-1, CNFs-2 and CNFs-3.

presence of some inorganic salts in the carbonization process. Raman spectroscopy is also performed for a better understanding of the graphite crystallite transformation (Fig. 4(b)). The two characteristic bands of CNFs at around 1360 and 1610 cm^{-1} correspond to the D-band and G-band, respectively. The D-band is assigned to a disordered carbon structure attributed to the breathing modes of sp^2 atoms in the aromatic ring, whereas the G-band is associated with the sp^2 stretching vibration of a perfect graphitic carbon structure. Based on a Lorentzian line shape of each sample, the peak heights for both D and G-bands are evaluated to calculate the I_D/I_G ratio.[30–32] The I_D/I_G values of CNFs-1, CNFs-2, and CNFs-3 are 0.79, 0.95, and 0.90, respectively. It was clearly observed that the addition of H_3PO_4 influences the graphitization of CNFs. This can be demonstrated by the significant changes in the I_D/I_G values. The higher I_D/I_G resulting from a decrease of the crystalline sp^2 domains of CNFs reduced the degree of graphitization. On the other hand, phosphorus atoms were introduced into carbon nanofibers as active sites in the form of doping. The formation of mesopores improved the specific surface area of the materials, which is conducive to the subsequent application of electrochemical signal detection. Additionally, the full width at half maximum (FWHM) of the D and G-bands is also employed as a major parameter for estimating the degree of structural order. As indicated in Table 1, the D-band FWHM of the CNFs decreases, whereas the G-band FWHM obviously increases with the increase of the phosphorylated lignin content.[33] This result is attributed to the introduction of the phosphorylated lignin, which promotes the dehydration and carbonization for bio-macromolecules at high temperatures to form a large number of aromatic carbon structures.

The properties of nitrogen and oxygen on the surface of carbon materials are further tested by XPS analysis (Fig. 5). XPS

Table 1 XRD and Raman parameters of the flexible CNFs

Codes	d_{002} (nm)	L_{002} (nm)	L_{100} (nm)	I_D/I_G	D-band FWHM (cm^{-1})	G-band FWHM (cm^{-1})
CNFs-1	0.3801	0.0434	0.0456	0.79	306.8	87.2
CNFs-2	0.3808	0.0431	0.0455	0.95	305.1	101.8
CNFs-3	0.3981	0.0429	0.0453	0.90	303.7	104.3

investigation confirms the existence of C, N and O. According to the spectra of each element, carbon is the main component of CNFs (85.49–93.33 at%) with a small amount of nitrogen (2.2–2.83 at%) and oxygen (3.5–3.7 at%). The C 1s peak is composed of five individual peaks (Fig. 5(b)), corresponding to C–S (~284.2 eV), C–C (~284.7 eV), C–N (~285.3 eV), C–O (~285.8 eV), and COOR (~289.1 eV) binding. The high resolution N 1s spectrum (Fig. 5(c)) is divided into four single peaks: pyridinic-N (~398.3 eV), pyrrolic/pyridinic-N (~400.1 eV), quaternary-N (~401.3 eV) and pyridinic-N oxide (~403.2 eV). Pyridinic-N and pyrrolic/pyridinic-N accounted for more than 65% of total nitrogen atoms. High content of pyridinic-N and pyrrolic/pyridinic-N have electrochemical activity in alkaline aqueous solution and provides the main pseudo capacitance, which is of great significance for improving the capacitance.[31,32] In addition, the presence of quaternary-N embedded in the carbon matrix and combined with three carbon atoms effectively promotes electron transfer and improves the electrical conductivity of carbon materials. There are also three fitted peaks in the O 1s spectrum (Fig. 5(d)), which may respectively represent C═O (~532.5 eV), C–O (~533.1 eV), and COOR (534.0 eV) bands. The nitrogen-containing and oxygen-containing functional groups on the surface of CNFs not only produce huge pseudo-capacitance, but also improve the wettability of the biomass-based CNF electrode in aqueous solution and the electrochemical properties of the material. The P 2p peak of CNFs-3 is shown in Fig. S4 (ESI†), It's obvious that the peaks of P═O and C_3PO signals appeared. This indicates the formation of phospholipid bonds between biomass molecules. This result also explains why the thermal stability of phosphated lignin is improved.

The cyclic compression–release performance of CNFs-3 proves its flexibility (Fig. 6(a)). A movie (Movie S1, ESI†) demonstrates that a circular ring made of independent CNFs-3 (1×1 cm^2) immediately recovers its original shape when lifting a weight of 200 g (500 times heavier than itself), showing striking shape-memory performance. Due to the existence of fibrous structural defects, CNFs-1 and CNFs-2 cannot show flexibility in the compression-release process. Moreover, CNFs-3 is superhydrophobic with water contact angles (WCA) of >130°. It exhibits extremely low water adhesion (Movie S2, ESI†), revealing self-cleaning capability of wearable electronics (Fig. 6(b)). In order to further demonstrate that CNFs can recover its original shape after a certain compression, the relative SEM image is shown in Fig. S5 (ESI†). The morphology of CNFs remains intact without obvious fracture. These properties are of great significance for the application of CNFs in flexible carbon materials.

In the 3D carbon nanofiber structure, the synergistic effect of ionic conductivity and specific surface area plays an important part in optimizing the electrochemical performance. With regards to electrical conductivity, as shown in Fig. S6 (ESI†), CNFs-3

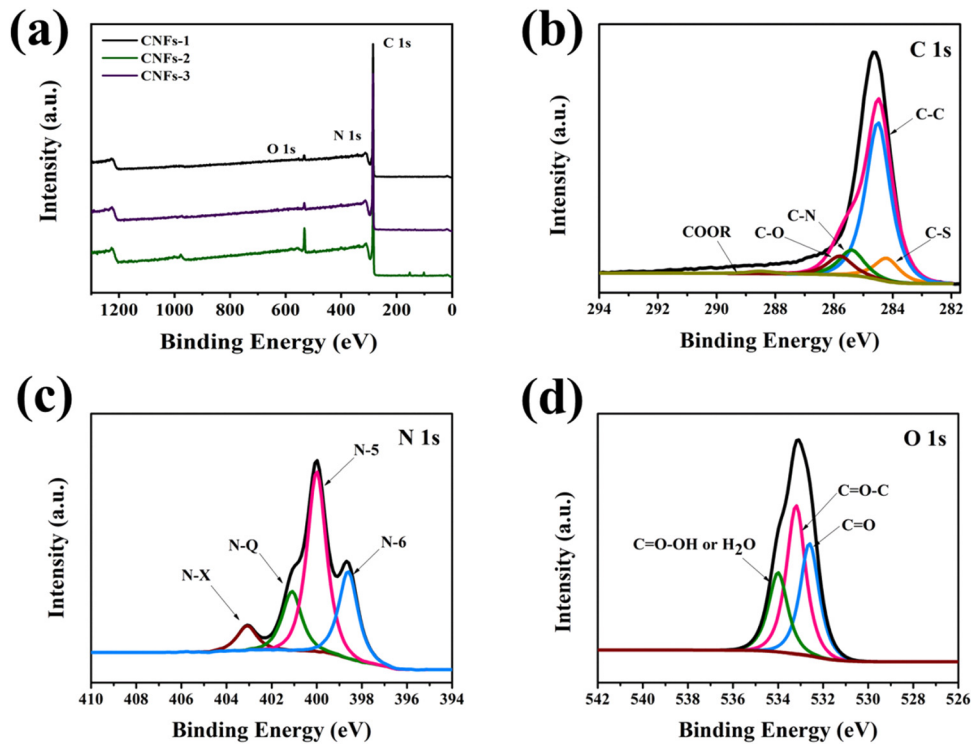

Fig. 5 Surface composition analysis of the biomass-based CNFs (a) XPS survey spectra of the biomass-based CNFs prepared with different samples, (b) C 1s, (c) O 1s, and (d) N 1s XPS spectra of CNFs-3.

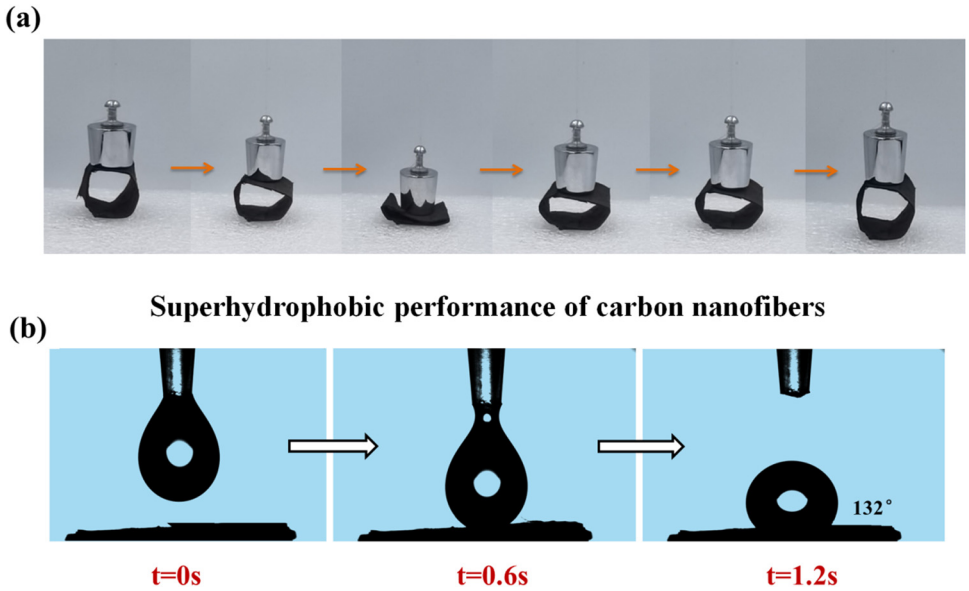

Fig. 6 Mechanical properties and surface wettability of the carbon nanofibers (a) a set of real-time images showing the flexibility of CNFs (top), and (b) optical images of water spreading on the surface of CNF membranes.

exhibits an electrical conductivity of 0.1305 S cm^{-1}, which is more than 1.2 times that of CNFs-1 (0.1026 S cm^{-1}). The specific surface areas of CNFs-1, CNFs-2 and CNFs-3 are 339.1, 345.6 and 472.8 $m^2 g^{-1}$, respectively. With the increase in the content of phosphorylated lignin, the interaction between bio-macromolecules is strengthened. This interaction structure can efficiently reduce the appearance of phase separation and obtain complete and uniform fibrous morphology, thus improving the specific surface area of carbon materials significantly. The electrochemical signal changes of different CNF electrode materials in PBS and urine solution are recorded by cyclic voltammetry (CV) to systematically analyze the feasibility of the CNF electrode.[34] As shown in Fig. 7(a)–(c), there is no obvious characteristic peak in the PBS solution while the redox peak can be observed in urine at a potential of 0.55 V, which is because uric acid responds only at a specific potential. The CV curves clearly indicate that the fabricated CNF electrode can be successfully applied to the detection of uric acid. The electron transfer process between the electrode material and the electrolyte

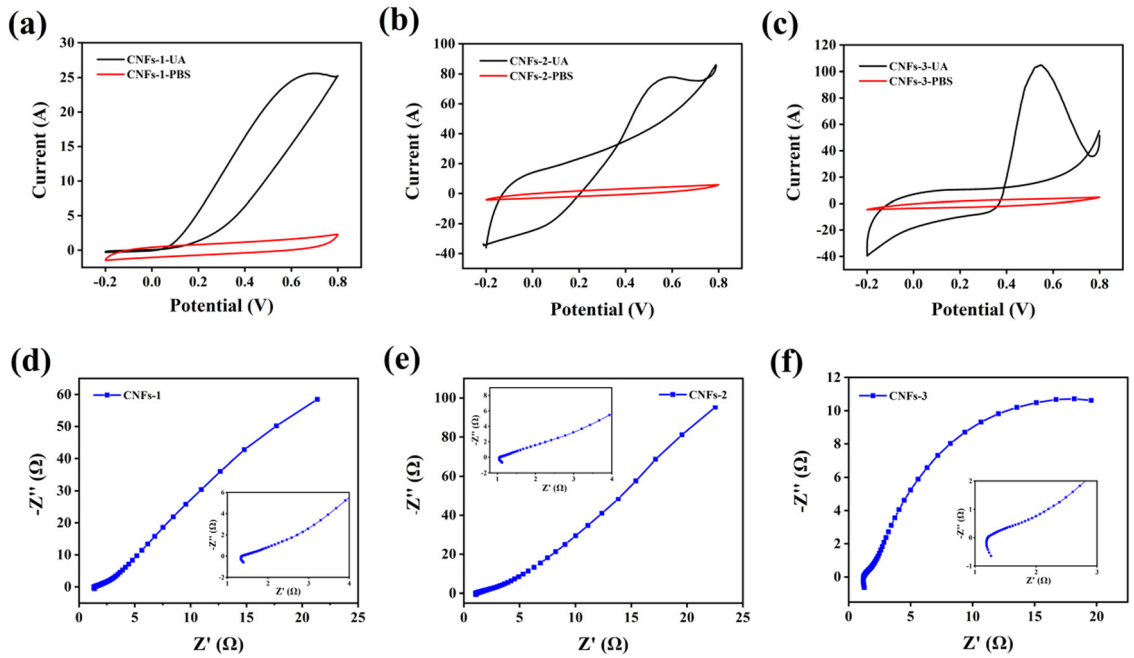

Fig. 7 (a)–(c) CV curves in PBS and uric acid solution of CNF electrodes with different masses of lignin, and (d)–(f) EIS curves of CNF electrodes with different masses of lignin.

during the charge–discharge process is further investigated by electrochemical impedance spectroscopy (EIS). As shown in Fig. 7(d)–(f), the EIS curves consisted of a semicircle and a straight line part, which accordingly correspond to charge-transfer resistance and diffusion process, respectively. The CNFs-3 has remarkable electrochemical performance, which is mainly attributed to its abundant functional groups, short ion transport channel and porous structure, which plays a positive role in improving the specific surface area of electroactivity, charge transfer and ion diffusion. The electron transfer process between the electrode material and the electrolyte during the charge–discharge process is further investigated by electrochemical impedance spectroscopy (EIS). CNFs-3 shows a smaller equivalent series resistance (R_s) and charge transfer resistance (R_{ct}) compared with CNFs-1. Interestingly, the diffusion resistance of CNFs-3 has a curve, mainly for two reasons: (i) the electrode surface is rough so that the diffusion process is partially equivalent to spherical diffusion and (ii) in addition to the electrode potential, some other state variables cause inductive reactance during the test.

The biosensor electrode is used to detect diverse concentrations of uric acid in artificial urine. The current output of the biosensor is recorded starting at 20 s, and the dependence of duration time on the current output is plotted in Fig. 8(a)–(c). Experimental findings indicated that the output signals were stable and reliable and there was a positive linear correlation between the current output and the gradient concentration of uric acid. Corresponding calibration plots of the biosensor are shown in Fig. 8(d)–(f). For the CNFs-2 electrode, the linear relationship can be described by $Y = 1.22 \times 10^{-}X + 93.48$ with the best correlation coefficient (R^2) of 0.967. As for the CNFs-3 electrode, the linear relationship can be expressed by $Y = 1.28 \times 10^{-2}X + 124.9$ with an R^2 of 0.979. However, the CNFs-1 electrode possessed a poor sensing performance and the linear relationship can be described by $Y = 8.74 \times 10^{-3}X + 50.81$ with the worst correlation coefficient (R^2) of 0.907. This is due to its poor electrical conductivity. The result proved that the fabricated CNFs could be an ideal working electrode material to construct the wearable sweat biosensor for uric acid detection in urine.

Furthermore, the fiber based wearable biosensor is finally assembled by attaching the CNFs to a commercial electrode, which possesses mechanical stability and structural integrity in the presence of large deformation or bending.[35–38] The relevant experimental studies are shown in Fig. S7 (ESI†). The wearable biosensor is used to detect uric acid in artificial urine, and the duration time is recorded in Fig. 9. The largest output current that could be achieved by the CNF-3 biosensor is 192 μA, which is mainly due to its good fiber morphology, regular graphitic structure and high conductivity (Fig. 9(a) and (b)). The softness and foldability of CNFs are important conditions for wearable electrodes. As shown in Fig. 9(c) and (d), all samples showed significant responses to external stimuli. In particular, the CNFs-3 biosensor shows the highest sensitivity and output current at different bending angles and pressures (Fig. S8, and Movie S3–S5, ESI†). This is mainly because the stress from bending presses the electrode firmly against the fabric, bringing it into closer contact with urine. Therefore, the biosensor generates more energy than the regular structure. Compared to other flexible electrode materials that show only limited bending, this biomass-based CNF electrode exhibits a much better mechanical flexibility and a broad application prospect in flexible wearable, electronic skin, flexible sensing and other fields.[3,9,12] Mechanical testing and cyclic loading are measured

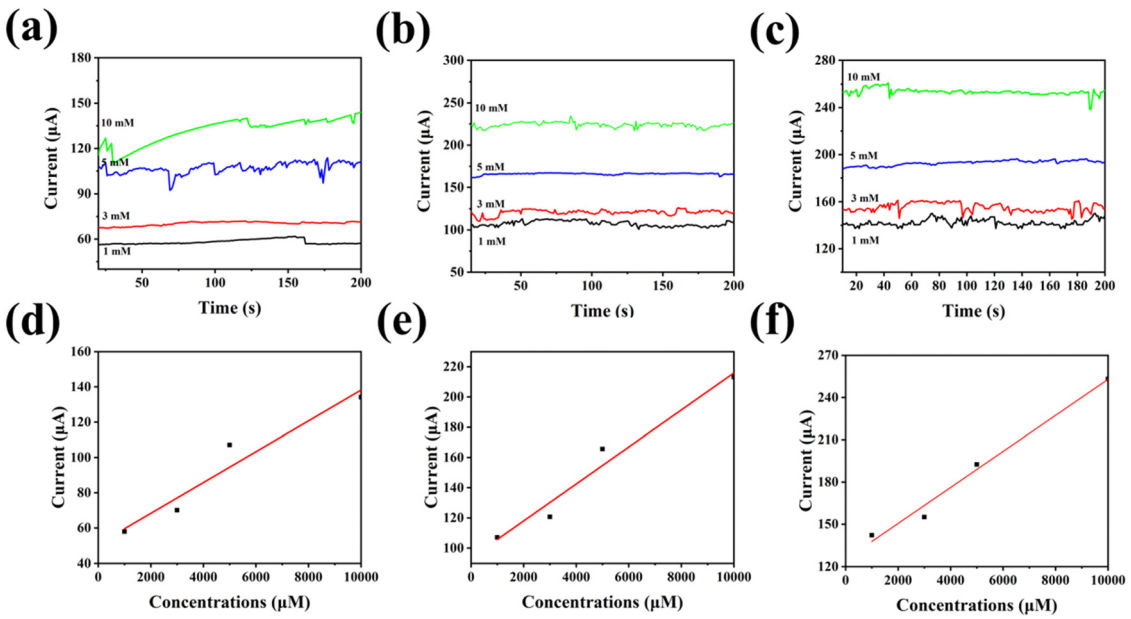

Fig. 8 (a)–(c) Uric acid detection of the wearable biosensor in artificial urine containing various concentrations. (d)–(f) Corresponding calibration plots of the wearable biosensors constructed with CNF electrodes at different ratios of phosphating lignin.

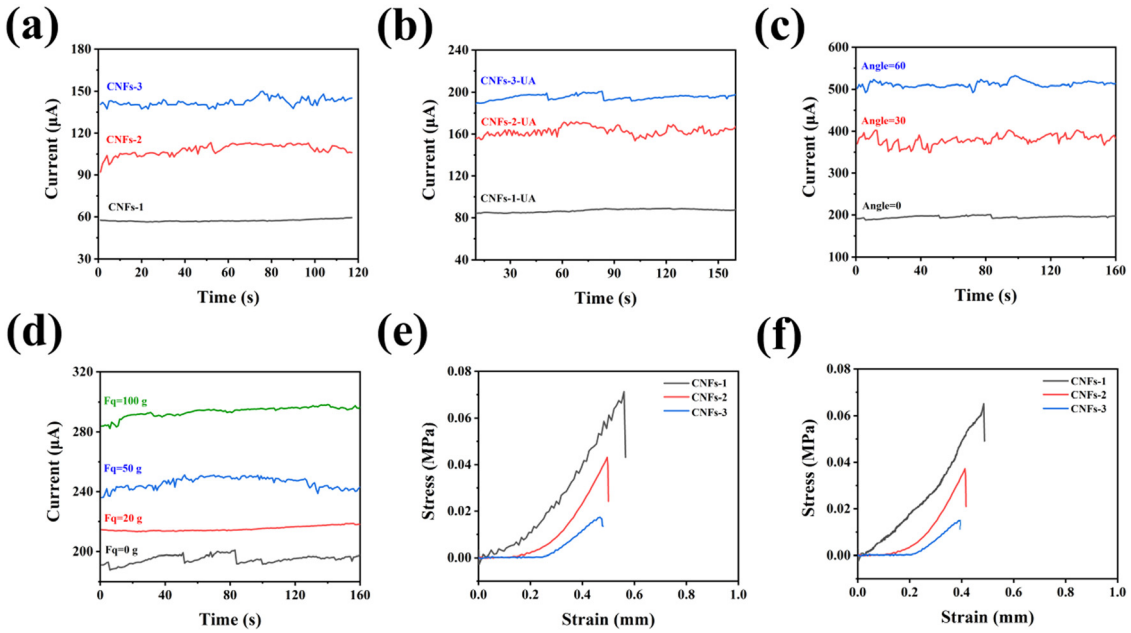

Fig. 9 (a) Output current detection of a wearable biosensor, (b) uric acid detection of the wearable biosensor in artificial urine, (c) sensitivity test of the CNFs-3 wearable biosensor with different bending degrees, (d) uric acid signal detection by the biosensor under different pressures, and (e), (f) microtensile–strain curve of the free-standing carbon nanofibers before and after repeated folding for 100 times.

to quantify mechanical performance. The compressive stress–strain curves are shown in Fig. 9(e) and (f). At the beginning of stress–strain curves, the rising trend is slow, and then rises sharply, indicating ideal compressive strength. Obviously, the compressive strength increases with the increment of the phosphorylated lignin content. For CNFs-1, the compressive strength is 2.59 MPa, while for CNFs-3 the compressive strength is 6.94 MPa, enhanced by 167.9%. The strength of CNFs-3 is much higher than that of others. It is noted that their moduli increased with the increase of the phosphorylated lignin content. Moreover, after repeated folding 100 times, the strength decreases only slightly. This phenomenon could be attributed to the strong cross-linking action between phosphorylated lignin and CA, resulting in a higher compressive strength. In addition, this biosensor can perform multifunctional sensing by observing dynamic physiological changes without expensive equipment or professional personnel (Fig. S9, ESI†). Wearable biosensors are an attractive candidate to solve the limitations of the traditional disease-centered and reactive medical model. This non-invasive technology provides a promising alternative strategy for the prevention and treatment of specific diseases.

4. Conclusion

In summary, a simple phosphating strategy is presented for preparing green and flexible CNFs by the electrospinning technique. The introduction of phosphated lignin effectively increases the molecular interaction in the electrospinning system, which avoids the microstructure collapse of biomass-based CNFs in the carbonization process. The obtained biomass-based CNFs exhibit good flexibility, higher content of carbon element, better electrical conductivity, and excellent electrochemical performance. The prepared CNFs can serve as a superior working electrode in an electrochemical biosensor to sensitively detect uric acid molecules in artificial urine. The result shows that the sensitive reaction of the CNFs-3 electrode is rapid, which can be installed on the diaper to facilitate monitoring by caregivers. These high properties are mainly attributed to the complete and uniform fibrous structure of biomass-based CNFs. This work paves the way for creating such exceptional carbon nanomaterials and opens up numerous opportunities for applications in environment, energy, electronics and bioengineering.

Conflicts of interest

There are no conflicts to declare.

Acknowledgements

This study was supported by the National Natural Science Foundation of China (No. 22278048, 31800498, 22078035, and 21908014), the Natural Science Foundation of Liaoning Province of China (No. LJKZ0543), the Open Fund of Jiangsu Provincial Key Laboratory of Pulp and Paper (No. KL201903), the Foundation (No. 2021KF07) of Guangxi Key Laboratory of Clean Pulp & Papermaking and Pollution Control, and the College of Light Industry and Food Engineering, Guangxi University.

References

1 Q. Zhu, Y. Jin, W. Wang, G. Sun and D. Wang, Bioinspired smart moisture actuators based on nanoscale cellulose

materials and porous, hydrophilic evoh nanofibrous membranes, *ACS Appl. Mater. Interfaces*, 2019, **11**(1), 1440–1448.
2 P. Zhu, H. Ou, Y. Kuang, L. Hao, J. Diao and G. Chen, Cellulose nanofiber/carbon nanotube dual network-enabled humidity sensor with high sensitivity and durability, *ACS Appl. Mater. Interfaces*, 2020, **12**(29), 33229–33238.
3 H. Wang, H. Cheng, Y. Huang, C. Yang, D. Wang, C. Li and L. Qu, Transparent, self-healing, arbitrary tailorable moist-electric film generator, *Nano Energy*, 2020, **67**, 104238.
4 L. H. Li, M. M. Hao, X. Q. Yang, F. Q. Sun, Y. Y. Bai, H. Y. Ding, S. Q. Wang and T. Zhang, Sustainable and flexible hydrovoltaic power generator for wearable sensing electronics, *Nano Energy*, 2020, **72**, 104663.
5 I. Shitanda, Y. Fujimura, T. Takarada, R. Suzuki, T. Aikawa, M. Itagaki and S. Tsujimura, Self-powered diaper sensor with wireless transmitter powered by paper-based biofuel cell with urine glucose as fuel, *ACS Sens.*, 2021, **6**(9), 3409–3415.
6 Q. Lyu, B. Peng, Z. Xie, S. Du, L. Zhang and J. Zhu, Moist-Induced electricity generation by electrospun cellulose acetate membranes with optimized porous structures, *ACS Appl. Mater. Interfaces*, 2020, **12**(51), 57373–57381.
7 M. Q. Jian, C. Y. Wang, Q. Wang, H. M. Wang, K. L. Xia, Z. Yin, M. C. Zhang, X. P. Liang and Y. Y. Zhang, Advanced carbon materials for flexible and wearable sensors, *Sci. China Mater.*, 2017, **60**(11), 1026–1062.
8 S. Yang, C. Li, N. Wen, S. Xu, H. Huang, T. Cong, Y. Zhao, Z. Fan, K. Liu and L. Pan, All-fabric-based multifunctional textile sensor for detection and discrimination of humidity, temperature, and strain stimuli, *J. Mater. Chem. C*, 2021, **9**(39), 13789–13798.
9 K. Xu, Y. Fujita, Y. Lu, S. Honda, M. Shiomi, T. Arie, S. Akita and K. Takei, A wearable body condition sensor system with wireless feedback alarm functions, *Adv. Mater.*, 2021, **33**(18), 2008701.
10 Y. Pang, J. Jian, T. Tu, Z. Yang, J. Ling, Y. Li, X. Wang, Y. Qiao, H. Tian, Y. Yang and T. L. Ren, Wearable humidity sensor based on porous graphene network for respiration monitoring, *Biosens. Bioelectron.*, 2018, **116**, 123–129.
11 C. Ma, M. G. Ma, C. Si, X. X. Ji and P. Wan, Flexible Mxene-based composites for wearable devices, *Adv. Funct. Mater.*, 2021, **31**(22), 2009524.
12 Z. Wang, Y. Si, C. Zhao, D. Yu, W. Wang and G. Sun, Flexible and washable poly(ionic liquid) nanofibrous membrane with moisture proof pressure sensing for real-life wearable electronics, *ACS Appl. Mater. Interfaces*, 2019, **11**(30), 27200–27209.
13 Y. Wang, L. Zhang, J. Zhou and A. Lu, Flexible and transparent cellulose-based ionic film as a humidity sensor, *ACS Appl. Mater. Interfaces*, 2020, **12**(6), 7631–7638.
14 H. Q. Wang, H. S. Luo, H. K. Zhou, X. D. Zhou, X. X. Zhang, W. J. Lin, G. B. Yi and Y. H. Zhang, Dramatically enhanced strain- and moisture-sensitivity of bioinspired fragmentized carbon architectures regulated by cellulose nanocrystals, *Chem. Eng. J.*, 2018, **345**, 452–461.
15 H. Wang, Y. Sun, T. He, Y. Huang, H. Cheng, C. Li, D. Xie, P. Yang, Y. Zhang and L. Qu, Bilayer of polyelectrolyte films for spontaneous power generation in air up to an integrated 1000 V output, *Nat. Nanotechnol.*, 2021, **16**(7), 811–819.
16 C. Wang, X. Li, E. Gao, M. Jian, K. Xia, Q. Wang, Z. Xu, T. Ren and Y. Zhang, Carbonized silk fabric for ultrastretchable, highly sensitive, and wearable strain sensors, *Adv. Mater.*, 2016, **28**(31), 6640–6648.
17 Z. Sun, L. Feng, C. Xiong, X. He, L. Wang, X. Qin and J. Yu, Electrospun nanofiber fabric: An efficient, breathable and wearable moist-electric generator, *J. Mater. Chem. A*, 2021, **9**(11), 7085–7093.
18 Z. Sun, L. Feng, X. Wen, L. Wang, X. Qin and J. Yu, Nanofiber fabric based ion-gradient-enhanced moist-electric generator with a sustained voltage output of 1.1 volts, *Mater. Horiz.*, 2021, **8**(8), 2303–2309.
19 B. C. Shiu, J. C. Jhang, T. T. Li, H. K. Peng, L. W. Wu, C. W. Lou and J. H. Lin, Using antibacterial fibers and metallic wires to make woven fabrics used as smart diapers, *J. Ind. Text.*, 2020, 1–14.
20 D. Shen, M. Xiao, G. Zou, L. Liu, W. W. Duley and Y. N. Zhou, Self-powered wearable electronics based on moisture enabled electricity generation, *Adv. Mater.*, 2018, **30**(18), 1705925.
21 M. Li, L. Zong, W. Yang, X. Li, J. You, X. Wu, Z. Li and C. Li, Biological nanofibrous generator for electricity harvest from moist air flow, *Adv. Funct. Mater.*, 2019, **29**(32), 1901798.
22 H. Lai, H. Zhuo, Y. Hu, G. Shi, Z. Chen, L. Zhong and M. Zhang, Anisotropic carbon aerogel from cellulose nanofibers featuring highly effective compression stress transfer and pressure sensing, *ACS Sustainable Chem. Eng.*, 2021, **9**(29), 9761–9769.
23 P. He, J. Wu, X. Pan, L. Chen, K. Liu, H. Gao, H. Wu, S. Cao, L. Huang and Y. Ni, Anti-freezing and moisturizing conductive hydrogels for strain sensing and moist-electric generation applications, *J. Mater. Chem. A*, 2020, **8**(6), 3109–3118.
24 M. Zhu, H. Liu, Q. Cao, H. Zheng, D. Xu, H. Guo, S. Wang, Y. Li and J. Zhou, Electrospun lignin-based carbon nanofibers as supercapacitor electrodes, *ACS Sustainable Chem. Eng.*, 2020, **8**(34), 12831–12841.
25 H. Zheng, X. Han, Q. Wei, C. Zheng, C. Huang, Z. Jin, Y. Li and J. Zhou, Biomass-based flexible fire warning sensor with excellent flame retardancy and sensitivity, *Chem. Eng. J.*, 2022, **437**, 135412.
26 H. Zheng, Q. Cao, M. Zhu, D. Xu, H. Guo, Y. Li and J. Zhou, Biomass-based flexible nanoscale carbon fibers: Effects of chemical structure on energy storage properties, *J. Mater. Chem. A*, 2021, **9**(16), 10120–10134.
27 Q. Cao, M. Zhu, J. Chen, Y. Song, Y. Li and J. Zhou, Novel lignin-cellulose-based carbon nanofibers as high-performance supercapacitors, *ACS Appl. Mater. Interfaces*, 2020, **12**(1), 1210–1221.
28 H. Liu, Z. Dai, Q. Cao, X. Shi, X. Wang, H. Li, Y. Han, Y. Li and J. Zhou, Lignin/polyacrylonitrile carbon fibers: The effect of fractionation and purification on properties of derived carbon fibers, *ACS Sustainable Chem. Eng.*, 2018, **6**(7), 8554–8562.
29 Z. Dai, X. Shi, H. Liu, H. Li, Y. Han and J. Zhou, High-strength lignin-based carbon fibers *via* a low-energy method, *RSC Adv.*, 2018, **8**(3), 1218–1224.
30 Y. Xiao, Y. Xu, K. Zhang, X. Tang, J. Huang, K. Yuan and Y. Chen, Coaxial electrospun free-standing and mechanically

stable hierarchical porous carbon nanofiber membranes for flexible supercapacitors, *Carbon*, 2020, **160**, 80–87.

31 N. Yu, H. Yin, W. Zhang, Y. Liu, Z. Tang and M.-Q. Zhu, High-Performance fiber-shaped all-solid-state asymmetric supercapacitors based on ultrathin MnO_2 nanosheet/carbon fiber cathodes for wearable electronics, *Adv. Energy Mater.*, 2016, **6**(2), 1501458.

32 F. J. García-Mateos, R. Berenguer, M. J. Valero-Romero, J. Rodríguez-Mirasol and T. Cordero, Phosphorus functionalization for the rapid preparation of highly nanoporous submicron-diameter carbon fibers by electrospinning of lignin solutions, *J. Mater. Chem. A*, 2018, **6**(3), 1219–1233.

33 S. Liu, X. Cheng, Z. He, J. Liu, X. Zhang, J. Xu and C. Lei, Amine-terminated highly cross-linked polyphosphazene-functionalized carbon nanotube-reinforced lignin-based electrospun carbon nanofibers, *ACS Sustainable Chem. Eng.*, 2020, **8**(4), 1840–1849.

34 X. Wu, D. Yang, C. Wang, Y. Jiang, T. Wei and Z. Fan, Functionalized three-dimensional graphene networks for high performance supercapacitors, *Carbon*, 2015, **92**, 26–30.

35 G. Zan, T. Wu, F. Zhu, P. He, Y. Cheng, S. Chai, Y. Wang, X. Huang, W. Zhang, Y. Wan, X. Peng and Q. Wu, A biomimetic conductive super-foldable material, *Matter*, 2021, **4**(10), 3232–3247.

36 G. Zan, T. Wu, Z. Zhang, J. Li, J. Zhou, F. Zhu, H. Chen, M. Wen, X. Yang, X. Peng, J. Chen and Q. Wu, Bioinspired nanocomposites with self-adaptive stress dispersion for super-foldable electrodes, *Adv. Sci.*, 2022, **9**(3), e2103714.

37 G. Zan, T. Wu, W. Dong, J. Zhou, T. Tu, R. Xu, Y. Chen, Y. Wang and Q. Wu, Two-level biomimetic designs enable intelligent stress dispersion for super-foldable C/NiS nanofiber free-standing electrode, *Adv. Fiber Mater.*, 2022, **6**, 487.

38 S. Chai, G. Zan, K. Dong, T. Wu and Q. Wu, Approaching superfoldable thickness-limit carbon nanofiber membranes transformed from water-soluble PVA, *Nano Lett.*, 2021, **21**(20), 8831–8838.